Bubbles as a Means for the Deaeration of Water Bodies

Yuhang Zhang[1]; Gedi Zhou[2]; and Andrea Prosperetti[3]

Abstract: Occasional dissolved-air supersaturation—such as may occur, for instance, downstream of dams—is harmful to fish because it causes gas bubble disease. A counterintuitive but effective means of reducing dissolved air content is the injection of bubbles in the supersaturated water. The bubbles greatly increase the air–water surface area available for the exsolution of the dissolved air, bring the interface into direct contact with the supersaturated water, and mix the water with their ascensional motion. This paper is a computational study of the process. The results suggest that the method has great potential and may be effective in applications. **DOI: 10.1061/(ASCE)EE.1943-7870.0001205.** © *2017 American Society of Civil Engineers.*

Downloaded from ascelibrary.org by Universiteit Twente on 05/02/18. Copyright ASCE. For personal use only; all rights reserved.

Introduction

It has long been known that elevated gas supersaturation levels in water can cause gas bubble disease (GBD) in fish and lead to high mortality rates (Ebel 1969; Beiningen and Ebel 1970; Meekin and Turner 1974; Weitkamp and Katz 1980). This remains a persistent problem as witnessed by the recent literature (Huang et al. 2010; Skov et al. 2013; Feng et al. 2014; Wang et al. 2015).

In rivers there are essentially two major mechanisms leading to supersaturation. In the first, water spilled over spillways becomes highly aerated, and when it plunges deeply into the stilling basin the elevated hydrostatic head forces the air bubbles into solution. It is estimated that the supersaturation thus generated can extend for at least 10 km downstream of the dam (Johnson et al. 2004). Secondly, supersaturation conditions can be established due to the effects of barometric pressure and water temperature (e.g., near thermal effluents), which are inversely correlated with gas solubility.

In recirculating aquaculture systems excess levels of dissolved gas may occur as a result of aeration devices, temperature increase, photosynthesis, localized occurrences of denitrification, or insufficient degassing of makeup water.

Fish appear not to be harmed by moderate levels of supersaturation (e.g., Knittel et al. 1980; Hansen et al. 1999; Gunnarsli et al. 2008; Liu et al. 2015); supersaturations of 10% are tolerated by current regulations in the states of Washington and Oregon, among others (Pickett and Harding 2002). Tolerance for several hours of up to 15% supersaturation has also been reported (McGrath et al. 2006; Huang et al. 2010), but at higher levels fish mortality quickly becomes elevated.

[1]Ph.D. Student, Dept. of Mechanical Engineering, Johns Hopkins Univ., 230 Latrobe Hall, 3400 N. Charles St., Baltimore, MD 21218. E-mail: gedi.zhou@gmail.com

[2]Ph.D. Student, Dept. of Mechanical Engineering, Johns Hopkins Univ., 230 Latrobe Hall, 3400 N. Charles St., Baltimore, MD 21218. E-mail: zhngyuhng@gmail.com

[3]Dept. of Mechanical Engineering, Johns Hopkins Univ., 230 Latrobe Hall, 3400 N. Charles St., Baltimore, MD 21218; Dept. of Science and Technology, Univ. of Twente, Postbus 217, AE 7500, Enschede, Netherlands; presently, Professor, Dept. of Mechanical Engineering, Univ. of Houston, Houston, TX 772014 (corresponding author). E-mail: prosperetti@jhu.edu

Note. This manuscript was submitted on June 11, 2016; approved on November 9, 2016; published online on March 31, 2017. Discussion period open until August 31, 2017; separate discussions must be submitted for individual papers. This paper is part of the ***Journal of Environmental Engineering***, © ASCE, ISSN 0733-9372.

At the root of the problem is the very low molecular diffusivity of dissolved gases, typically on the order of 10^{-9} m^2/s. For this reason, the time necessary for dissolved gas to diffuse out of a 1-mm-thick layer of water, for example, exceeds 15 min, which increases to one day for a layer 10 mm thick. With its strong mixing, turbulence continually brings fresh liquid to the surface, but this so-called *surface renewal* mechanism is not sufficient to permit an adequately rapid degassing of the water. In the case of spills from reservoirs, operational regulation has been proposed to remedy the occurrence of supersaturation (Feng et al. 2014) but, due to its root in basic physical constraints, the problem has otherwise proven to be difficult to deal with it.

This paper describes a theoretical and computational study of an approach which, on first sight, may seem counterproductive—namely, the injection of small gas bubbles at some depth below the surface of the supersaturated water. The main reason for the effectiveness of this idea is that as these bubbles rise the excess dissolved gas will diffuse into them and vent to the atmosphere when they pop at the water surface. This paper shows that even with a relatively small amount of injected gas, a rapid and effective decrease of the dissolved gas can be achieved.

Physical Process

The effectiveness of bubble injection in promoting the deaeration of a supersaturated liquid rests on two basic mechanisms. In the first place, bubbles provide a large amount of surface area across which the dissolved gas can leave the liquid. For example, 0.5-mm-diameter bubbles distributed in 1 m^3 of liquid with a volume concentration of only 1% increase the available area for gas exchange 120 times over that of a plane 1 m^2 surface. Furthermore, in contrast with the free surface of the water, the air–water interface that the bubbles provide is in direct contact with the supersaturated liquid, which has the effect of dramatically shortening the diffusion times. Secondly, the rising bubbles cause a large-scale recirculatory motion in the water mass which enhances the surface renewal process caused by turbulent transport.

The concentration ρ_g^b of dissolved gas at the surface of a bubble is determined by Henry's law, according to which

$$\rho_g^b = K(T)p \tag{1}$$

where $K(T)$ = temperature-dependent parameter of Henry's law; and p = pressure in the bubble. The pressure in the bubble at any depth can be approximated as the local hydrostatic pressure because the effect of flow on the pressure makes an exceedingly

small difference as far as Eq. (1) is concerned. Because the hydrostatic pressure in water increases at a rate close to 0.1 atmospheres (atm) per meter, water which at normal atmospheric pressure would exhibit a 30% supersaturation would be saturated at a depth of 3 m. Bubbles injected below this depth would therefore be in an undersaturated liquid and would start to dissolve. In practice, bubbles could be injected somewhat below this depth if they were sufficiently large not to dissolve completely as they rose past the 3-m level. Even if a small amount of air would be added to the water during the ascent of the bubbles from the point of injection to the 3-m depth, the induced recirculation may be sufficiently strong to compensate for this negative effect.

This estimate neglects the effect of surface tension, which causes the pressure in the bubble to exceed that in the surrounding liquid by an amount equivalent to an extra depth $h = 4\sigma/(\rho g d)$, where σ is the surface tension coefficient, ρ is the water density, g is the acceleration of gravity, and d is the bubble diameter. For $d = 0.1$ mm, numerically this effect amounts to an extra depth of approximately 0.28 m, which therefore is small for bubbles of this size and becomes essentially negligible for larger bubbles.

There are, however, other reasons why the bubble size is important. One is a competition between the residence time in the water column, which decreases with increasing bubble size due to the increasing buoyant velocity, and the area provided for the bubble–liquid gas exchange, which increases with size. The effect of these competing trends is examined through a simple model for the rate at which a bubble absorbs dissolved gas, namely

$$\frac{dm_g}{dt} = \pi d^2 h(\rho_g^\infty - \rho_g^b) \tag{2}$$

where h = mass transfer coefficient; ρ_g^∞ = mass density of the gas dissolved in the liquid far from the bubble; and ρ_g^b = mass density of the dissolved gas at the bubble interface. Assuming $\rho_g^\infty \gg \rho_g^b$, this can be integrated from the initial depth of the bubble, $z = -Z_0$, to the free surface of the liquid, $z = 0$, to find an increase of the gas mass in the bubble given by

$$\Delta m_g = \pi \rho_g^\infty \int_{-Z_0}^{0} \frac{d^2(z)h(z)}{w_T(z)} dz \tag{3}$$

where w_T = terminal rise velocity of the bubble. A standard correlation for the mass transfer coefficient is

$$\mathrm{Sh} \equiv \frac{hd}{D} = 2 + 0.6\mathsf{R}_b^{1/2}\mathsf{Sc}^{1/3} \tag{4}$$

in which Sh = Sherwood number; $\mathsf{R}_b = dw_T/\nu$ is the bubble Reynolds number; and $\mathsf{Sc} = \nu/D$ is the liquid Schmidt number, where ν = kinematic viscosity and D = mass diffusivity. The terminal velocity can be found by balancing buoyancy and drag in the vertical direction

$$3\pi\mu d w_T f(\mathsf{R}_b) = \rho v g \tag{5}$$

where $v = (\pi/6)d^3$ is the bubble volume; g = acceleration of gravity; and

$$f(\mathsf{R}_b) = 1 + 0.15\mathsf{R}_b^{0.687} \tag{6}$$

is a correction to the Stokes law which approximately accounts for finite Reynolds number effects. It may be noted that, due to the dependence of f on the bubble Reynolds number, Eq. (5) is an implicit equation for w_T.

The integrand of Eq. (3) determined in this way is plotted as a function of the bubble diameter in Fig. 1. It is seen that there is a minimum around $d = 0.1$ mm, after which the curve quickly rises.

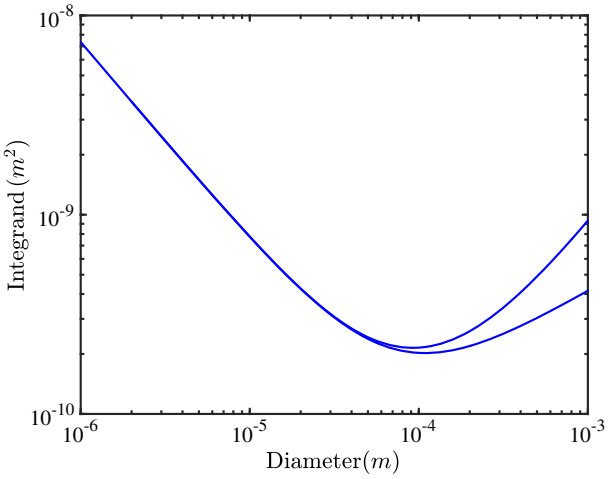

Fig. 1. Integrand of Eq. (3) versus bubble diameter; the increasing trend beyond approximately 0.1 mm diameter implies that, for an individual bubble, the effect of the shorter residence time due to a higher buoyant velocity is more than balanced by the increased area available for the transfer of gas out of the liquid into the bubble; the dashed line is obtained with the terminal velocity as predicted by Stokes's law; the solid line incorporates the finite Reynolds number correction incorporating the factor $f(\mathsf{R}_b)$ in Eq. (5)

For bubbles larger than this value, therefore, the reduced residence time caused by the increasing rise velocity is more than balanced by the increase in the bubble area. For a fixed bubble number, this result indicates that larger bubbles perform better than smaller ones. However, for a fixed total air injection rate, the bubble number increases with decreasing size, and smaller bubbles may be preferable. The optimum balance between these trends will be determined by practical considerations such as energy cost and the available equipment.

With their ascensional motion, the bubbles promote convective currents in the water body and thus intensify the surface renewal process caused by turbulence. The amount of this enhanced convection will strongly depend on the bubble size, which again points to this quantity as one of the key parameters in the design of an effective and efficient system.

Mathematical Models

This paper simulates the rise and diffusive growth of bubbles in a supersaturated liquid by using two different mathematical models. In view of the approximations that both models contain, the comparison of their results will give some assurance as to the reliability of the predictions. The first model is of the so-called Euler–Lagrange type: individual bubbles are tracked as they rise and scavenge the dissolved gas. The second model is of the Euler–Euler type: the bubbles are treated in an average sense as a continuum which interacts with the surrounding water. It is assumed that the liquid is at rest except for the rising bubbles, so that turbulence effects are negligible.

In both models it is assumed that the fraction of volume occupied by the bubbles is very small so that the mixture can be treated as incompressible. The equation of continuity reduces therefore to

$$\nabla \cdot \mathbf{u} = 0 \tag{7}$$

where $\mathbf{u}$ = liquid velocity field. The liquid momentum equation is written as

Downloaded from ascelibrary.org by Universiteit Twente on 05/02/18. Copyright ASCE. For personal use only; all rights reserved.

$$\rho\frac{d\mathbf{u}}{dt} = -\nabla p + \mu\nabla^2\mathbf{u} + \rho g + \mathbf{F}_{lb} \tag{8}$$

in which ρ = liquid density, taken as constant; p = pressure field; μ = viscosity; g = acceleration of gravity; and $\mathbf{F}_{lb}$ = force exerted by the bubbles on the liquid. This term is different in the two models and will be further specified below. The velocity derivative on the left-hand side is the Lagrangian derivative

$$\frac{d\mathbf{u}}{dt} = \frac{\partial\mathbf{u}}{\partial t} + (\mathbf{u}\cdot\nabla)\mathbf{u} \tag{9}$$

In both models, the gas diffusion process in the liquid is governed by the diffusion equation in the form

$$\frac{d\rho_g}{dt} = D\nabla^2\rho_g - \Gamma_{lb} \tag{10}$$

in which ρ_g = mass density of the gas dissolved in the liquid; $d\rho_g/dt$ = Lagrangian derivative defined similarly to Eq. (9); D = mass diffusivity; and Γ_{lb} = bubbles–liquid interaction term different in the two models.

Euler–Lagrange Model

In the Euler–Lagrange model, the bubbles are tracked individually in their motion and evolution. The velocity $\mathbf{w}$ of each bubble is governed by Newton's equation

$$\frac{d}{dt}(m_b\mathbf{w}) = 3\pi\mu d(\mathbf{u}-\mathbf{w})f(\mathsf{R}_b) + \frac{1}{2}\rho\left[v\left(\frac{d\mathbf{u}}{dt}-\frac{d\mathbf{w}}{dt}\right) + (\mathbf{u}-\mathbf{w})\frac{dv}{dt}\right] + (m_b-\rho v)\mathbf{g} \tag{11}$$

in which the liquid velocity $\mathbf{u}$ is evaluated at the bubble position. The first term on the right-hand side, aside from $f(\mathsf{R}_b)$, is the Stokes drag force on a spherical bubble. The factor was defined in Eq. (6) but because the liquid motion is now accounted for, the definition of the Reynolds number becomes

$$\mathsf{R}_b = \frac{d|\mathbf{w}-\mathbf{u}|}{\nu} \tag{12}$$

The second term on the right-hand side of Eq. (11) accounts for added mass effects and the last term is the effect of gravity, where m_b is the bubble mass. Because the bubble mass is very small, the terms containing this quantity (and, in particular, the left-hand-side of the equation) can be neglected, resulting in the approximation

$$3\pi\nu d(\mathbf{u}-\mathbf{w})f(\mathsf{R}_b) + \frac{1}{2}\left[v\left(\frac{d\mathbf{u}}{dt}-\frac{d\mathbf{w}}{dt}\right) + (\mathbf{u}-\mathbf{w})\frac{dv}{dt}\right] - v\mathbf{g} = 0 \tag{13}$$

Because the terms in Eq. (13) are the force exerted by the liquid on the bubble by the action-reaction principle, the direct force exerted by each bubble on the liquid vanishes. However, the interaction force $\mathbf{F}_{lb}$ in Eq. (8) does not vanish because it must account for the fact that the effective density of the bubbly liquid, ρ_e, is smaller than ρ, the density of the pure liquid, by the fraction of volume occupied by the bubbles. If the size of the bubbles is small, this effect can be incorporated into the equation by taking

$$\mathbf{F}_{lb} \simeq \sum_{i=1}^{N}\rho v_i\left(\frac{d\mathbf{u}}{dt}-\mathbf{g}\right)\delta(\mathbf{x}-\mathbf{x}_i) \tag{14}$$

in which δ = delta distribution and the sum is extended to all of the N bubbles. This expression can be justified by noting that the liquid in a volume $\mathcal{V}$ of the bubbly mixture occupies only a portion $\mathcal{V} - \sum_k v_k$ of $\mathcal{V}$, where v_k is the volume of the kth bubble in $\mathcal{V}$. Thus the liquid inertia in a volume $\mathcal{V}$ is given by

$$\int_{\mathcal{V}-\sum_k v_k}\rho\frac{d\mathbf{u}}{dt}d\mathcal{V} \simeq \int_{\mathcal{V}}\rho\frac{d\mathbf{u}}{dt}d\mathcal{V} - \sum_k\int_{v_k}\frac{d\mathbf{u}}{dt}dv_k \simeq \int_{\mathcal{V}}\rho\left[\frac{d\mathbf{u}}{dt} - \sum_k v_k\frac{d\mathbf{u}}{dt}\delta(\mathbf{x}-\mathbf{x}_k)\right]d\mathcal{V} \tag{15}$$

and similarly for the terms multiplied by g.

The equation governing the exchange of gas between each bubble and the liquid was given in Eq. (2), noting that in the expression for the mass transfer coefficient the bubble Reynolds number defined by Eq. (12) should be used. From the perfect gas equation of state

$$v = \frac{\mathcal{R}_g m_g T}{M_g p_g} \tag{16}$$

where $\mathcal{R}_g$ = universal gas constant; T = absolute temperature; M_g = molecular mass of the gas; and p_g = molecular pressure of the gas. Upon assuming isothermal conditions and differentiating, by Eq. (2)

$$\frac{dv}{dt} = \frac{\mathcal{R}_g T}{M_g p_g}\pi d^2 h(\rho_g^\infty - \rho_g^b) - \frac{\mathcal{R}_g T m_g}{M_g p_g^2}\mathbf{w}\cdot\nabla p_g \tag{17}$$

The pressure fluctuations due to the liquid motion in the neighborhood of the bubble are much smaller than the local hydrostatic pressure. Therefore in Eq. (17) we assume that the gas pressure balances the hydrostatic pressure in the liquid so that $\nabla p_g \simeq \rho\mathbf{g}$ and $p_g = p_0 - \rho g z$, where $z < 0$ is the depth of the bubble. Then

$$\frac{dv}{dt} = \frac{\mathcal{R}_g T}{M_g(p_0-\rho g z)}\pi d^2 h(\rho_g^\infty - \rho_g^b) - \frac{v}{p_0-\rho g z}\rho\mathbf{w}\cdot\mathbf{g} \tag{18}$$

Because the temperature is uniform, $(\mathcal{R}_g T/M_g) = p_0/\rho_0$, where ρ_0 is the air density at ambient pressure (i.e., above the water surface at $z = 0$), so the equation can be re-cast in the more convenient form

$$\frac{dv}{dt} = \frac{H}{H-z}\pi d^2 h\frac{\rho_g^\infty - \rho_g^b}{\rho_0} + \frac{v}{H-z}w_z \tag{19}$$

where $H = p_0/\rho g \simeq 10.3$ m; and w_z = vertical component of the bubble velocity. By expressing the bubble volume in terms of its diameter, the bubble diameter can be calculated from Eq. (19).

The dissolved gas density at the bubble surface ρ_g^b can be obtained from Henry's law [Eq. (1)], again with the assumption that the pressure in the bubble is essentially hydrostatic so that $\rho_g^b = K(T)(p_0 - \rho g z)$. If ρ_g^0 is the saturated dissolved gas density at $z = 0$, this may be written as

$$\rho_g^b = \left(1 - \frac{z}{H}\right)\rho_g^0 \tag{20}$$

In the Euler–Lagrange model, on the basis of an argument similar to that leading to Eq. (14), the source term Γ_{lb} in the diffusion equation in the liquid [Eq. (10)] is

Downloaded from ascelibrary.org by Universiteit Twente on 05/02/18. Copyright ASCE. For personal use only; all rights reserved.

$$\Gamma_{lb} = -\sum_{i=1}^{N}\left(v_i\frac{d\rho_g}{dt} - \frac{dm_{g,i}}{dt}\right)\delta(\mathbf{x}-\mathbf{x}_i) \tag{21}$$

In the second term, $m_{g,i} = \rho_{g,i}v_i$, where $\rho_{g,i}$ is the density of the gas in the bubble, and in the first term ρ_g is the density of the gas dissolved in the liquid. Because the latter is much smaller than the former, the first term can be dropped, and Γ_{lb} reduces to

$$\Gamma_{lb} \simeq \sum_{i=1}^{N}\frac{dm_{g,i}}{dt}\delta(\mathbf{x}-\mathbf{x}_i) \tag{22}$$

where $dm_{g,i}/dt$ is given by Eq. (2).

In the Euler–Lagrange model the bubbles are generated at random points on a horizontal surface immersed in the water. They are all injected with the same initial diameter d_0 at their terminal velocity given by Eq. (5) to avoid the accumulation that would result if they were to accelerate starting from zero velocity (Oresta and Prosperetti 2013).

Euler–Euler Model

In the Euler–Euler model the bubbles are considered as a continuum intermixed with the water. Their concentration is expressed in terms of the number density $n(\mathbf{x}, t)$ which satisfies a conservation law of the form

$$\frac{\partial n}{\partial t} + \nabla\cdot(n\mathbf{w}) = \dot{n}_s \tag{23}$$

Here $\mathbf{w} = \mathbf{w}(\mathbf{x}, t)$ is the bubble velocity, which in this model is a field defined everywhere in the domain and can be interpreted as the mean velocity of the bubbles contained in an averaging volume centered at $\mathbf{x}$. The term $\dot{n}_s$ on the right-hand side is nonzero only in the small fraction of the computational domain occupied by the bubbler and mimics the introduction of bubbles into the system. It is modeled as

$$\dot{n}_s = \sqrt{\frac{\pi}{2}}\frac{\dot{n}_A}{16\sigma_z}\exp\left[-\frac{(z-z_0)^2}{2\sigma_z^2}\right]\left(1+\tanh\frac{x-L_{x1}}{\varepsilon_x}\right) \times\left(1+\tanh\frac{L_{x2}-x}{\varepsilon_x}\right)\left(1+\tanh\frac{y-L_{y1}}{\varepsilon_y}\right)\left(1+\tanh\frac{L_{y2}-y}{\varepsilon_y}\right) \tag{24}$$

The bubbler extends over the area $A = (L_{x2}-L_{x1})(L_{y2}-L_{y1})$ corresponding to $L_{x1} < x < L_{x2}$ and $L_{y1} < y < L_{y2}$, and is symmetric about its midplane located at a depth z_0. The numbers ε_x, ε_y, and σ_z are small constants which smooth the edges of the bubbler. This form is adopted to avoid sharp discontinuities in the bubble number density at the edges of the bubbler, which have an adverse effect on numerical stability. In order to see the physical significance of $\dot{n}_s$, integrate Eq. (24) over the liquid volume. If the bubbler is located at the bottom of the domain so that $z_0 = 0$, because σ_z is small, the integration over z can be extended from 0 to infinity to find

$$\int_0^\infty dz\int_A \dot{n}_s dA = \dot{n}_A A \tag{25}$$

where $\dot{n}_A$ = number of bubbles introduced by the bubbler per unit area and unit time. If z_0 is located above the bottom at a distance $z_0 \gg \sigma_z$ from it, then the z integration approximately extends from minus infinity to infinity and the right-hand side of Eq. (25) is multiplied by 2 so that $\dot{n}_A$ is half the number of bubbles introduced per unit bubbler area and unit time.

In Eq. (23) for the bubble number density, coalescence and splitting have been neglected, the former because of the small bubble concentration. Bubble splitting would be significant in weak turbulence only for bubbles of several millimeters in diameter or larger, which are not beneficial for the deaeration process and accordingly are not considered here.

Given that the liquid is quiescent except for the flow induced by the bubbles, the mean acceleration to which the bubbles are subjected is very small and therefore the added mass effects on the average bubble motion can be neglected. [In the Euler–Lagrange model individual bubbles may be subjected to significant accelerations, and for this reason mass has been retained in Eq. (11).] The bubble motion is therefore the result of a balance of drag and buoyancy

$$3\pi\nu d(\mathbf{u}-\mathbf{w})f(\mathsf{R}_b) = v\mathbf{g} \tag{26}$$

or

$$\mathbf{w} = \mathbf{u} - w_T\frac{\mathbf{g}}{g} \tag{27}$$

where w_T = terminal velocity introduced in Eq. (5). This relation expresses the bubble velocity field as the sum of the local water velocity and of the terminal velocity in a quiescent fluid.

The mass conservation equation for the bubble phase is

$$\frac{\partial}{\partial t}(\alpha\rho_g^b) + \nabla\cdot(\alpha\rho_g^b\mathbf{w}) = n\frac{dm_g}{dt} = \pi n d^2 h(\rho_g^\infty - \rho_g^b) \tag{28}$$

in which $\alpha = nv$ is the bubble volume fraction; and on the right-hand side dm_g/dt is expressed using Eq. (2). The gas density here is simply calculated using the hydrostatic balance as before and is given by Eq. (20).

The interaction force in the liquid momentum Eq. (8) is calculated using a volume-averaged form of Eq. (14), namely

$$\mathbf{F}_{lb} = \alpha\rho\left(\frac{d\mathbf{u}}{dt} - \mathbf{g}\right) \tag{29}$$

The term Γ_{lb} in the liquid diffusion equation [Eq. (10)] is given similarly by

$$u^*\Gamma_{lb} = n\frac{dm_g}{dt} = \pi n d^2 h(\rho_g^\infty - \rho_g^b) \tag{30}$$

Numerical Aspects

For both the Euler–Lagrange and the Euler–Euler models the flow solver is based on a standard projection method on a regular grid with a staggered arrangement for the dependent variables (e.g., Fletcher 1988; Ferziger and Periç 2002). The intermediate velocity field is found from

$$\mathbf{u}^* = \mathbf{u}^n + \Delta t[-(\nabla\cdot\mathbf{u}\mathbf{u})^{n+1/2} + \nu(\nabla^2\mathbf{u})^{n+1/2}] \tag{31}$$

in which Δt = time step; and the superscript $n+1/2$ denotes intermediate values found with the second-order Adams–Bashforth time integration. The end-of-time step velocity is given by

$$\mathbf{u}^{n+1} = \mathbf{u}^* - \frac{\Delta t}{\rho_f}\nabla p^{n+1/2} \tag{32}$$

with the pressure calculated from the Poisson equation

Downloaded from ascelibrary.org by Universiteit Twente on 05/02/18. Copyright ASCE. For personal use only; all rights reserved.

$$\nabla^2 p^{n+1/2} = \rho_f \frac{\nabla \cdot \mathbf{u}^*}{\Delta t} \tag{33}$$

Second-order accurate central differences are used for the discretization of the differential operators. Stability of the time advancement is ensured by choosing the time step according to (e.g., Ferziger and Periç 2002)

$$\Delta t = \frac{C}{\sum_{i=1}^{3} \max|u_i|/\Delta x_i + 2\nu/\Delta x_i^2} \tag{34}$$

where $C < 1$ = constant which ensures numerical stability; index i runs over the three spatial directions; and Δx_i = mesh size in the ith direction.

The diffusion equation is discretized explicitly as

$$\frac{\rho_g^{n+1} - \rho_g^n}{\Delta t} + [\nabla \cdot (\mathbf{u}\rho_g)]^n = D(\nabla^2 \rho_g)^n \tag{35}$$

The convective terms are discretized according to the upwind rule and the diffusive terms by central differences. Stability of time advancement in this case requires a time step given by

$$\Delta t = \frac{C'}{\sum_{i=1}^{3} \max|u_i|/\Delta x_i + 2D/\Delta x_i^2 + u_i^2/2D} \tag{36}$$

where $C' < 1$. Because $D \ll \nu$, the time-step limit given by Eq. (36) is more stringent than that provided by Eq. (34). Set C and C' equal to 0.5.

The Euler–Lagrange model requires that the fluid velocity be evaluated at the bubble position. This objective is realized by a second-order Lagrangian interpolation using velocity values from the eight cells surrounding the cell containing the bubble.

Integration over a computational cell of the term $\mathbf{F}_{lb}$ given by Eq. (14) in the liquid momentum equation gives

$$\int_{V_{\text{cell}}} \mathbf{F}_{lb} dV_{\text{cell}} = \sum_k \rho v_k \left(\frac{d\mathbf{u}}{dt} - g\right) \tag{37}$$

with the summation extended to the bubbles centered in the cell. Special smoothing procedures may be needed to ensure stability at high volume fractions (Capecelatro and Desjardins 2013), but this has proven unnecessary in the present simulations.

A numerical difficulty is associated with the bubble equation of motion [Eq. (11)] due to the smallness of the characteristic time that it involves. Rewrite Eq. (11) in the form

$$\frac{d\mathbf{w}}{dt} + \left(\frac{1}{\tau} + \frac{1}{v}\frac{dv}{dt}\right)\mathbf{w} = \mathbf{f} \tag{38}$$

where

$$\frac{1}{\tau} = \frac{6\pi\nu d}{v} f(\mathsf{R}_b) \tag{39}$$

and

$$\mathbf{f} = \left[\frac{6\pi\nu d}{v} f(\mathsf{R}_b) + \frac{1}{v}\frac{dv}{dt}\right]\mathbf{u} + \frac{d\mathbf{u}}{dt} - 2g \tag{40}$$

According to Eq. (38), with τ approximately constant over a time step, the advanced-time velocity $\mathbf{w}^{n+1}$ is given by

$$v^{n+1}\mathbf{w}^{n+1} = e^{-\Delta t/\tau^n} v^n \mathbf{w}^n + \int_{t^n}^{t^{n+1}} e^{-(t^{n+1}-s)/\tau^n} v(s)\mathbf{f}(s) ds \tag{41}$$

Because the terms constituting $\mathbf{f}$ are slowly varying on the scale τ, this formula can be approximated as (e.g., Hochbruck and Ostermann 2010; Ireland et al. 2013)

$$v^{n+1}\mathbf{w}^{n+1} \simeq e^{-\Delta t/\tau^n} v^n \mathbf{w}^n + e^{-\Delta t/\tau^n} v^n \mathbf{f}^n \tag{42}$$

where $\Delta t = t^{n+1} - t^n$. All the simulations described subsequently use no-slip conditions at the bottom domain and periodicity conditions on the vertical boundaries. The free surface allows for free slip of the liquid (i.e., zero tangential stress) while the normal derivative of the vertical velocity and of the scalar fields is set to zero.

Comparison of the Euler–Lagrange and Euler–Euler Models

In view of the approximations contained in both the Euler–Lagrange and Euler–Euler models, it is interesting to carry out a direct comparison of the two. Agreement between the respective results would lend support to both approaches.

For this purpose a computational domain with a square cross section with sides $L = 0.2$ m and a height of $H = 0.5$ m was chosen. The domain was limited because its size was dictated by the need to limit the number of bubbles in the Euler–Lagrange simulation, which, with the computational resources employed, could not exceed approximately 10^7 bubbles. Both codes were tested with discretizations of $80 \times 80 \times 200$ and $100 \times 100 \times 250$ cells, finding indistinguishable results; the finer grid was used to obtain the results described here.

At the initial instant the water contained uniformly dissolved air 30% above the saturation level at 20°C, namely $\rho_g = 2.27 \times 10^{-5}$ kg/m^3. Gas was injected uniformly over the base of the domain at the rate $Q = 1.68 \times 10^{-6}$ m^3/s. The gas diffusivity in the liquid was $D = 2 \times 10^{-9}$ m^2/s and the numerical parameters in the bubbler model [Eq. (24)] were taken as $\varepsilon_x = \varepsilon_y = 0.01L$ and $\sigma_z = 0.002H$; the bubbler midplane was at the bottom.

Fig. 2 shows a comparison of the results given by the two models for initial bubble diameters ranging from 0.2 to 1 mm, keeping

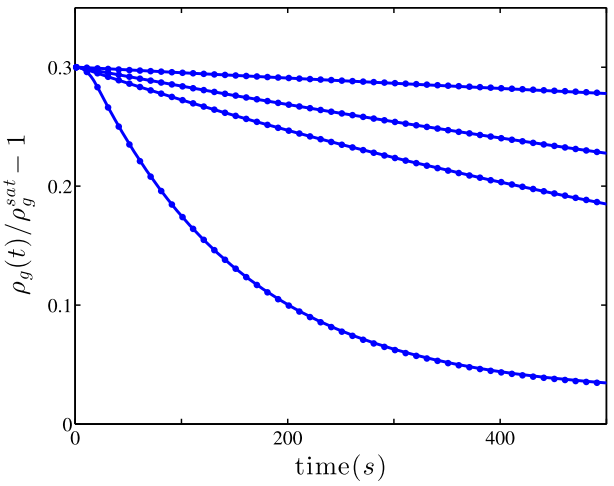

Fig. 2. Decrease of the whole-domain, volume-averaged water supersaturation as a function of time for different initial sizes of the injected bubbles and a fixed gas flow rate; the bubble diameters are, in ascending order, 0.2, 0.4, 0.5, and 1 mm; the continuous lines show the results of the Euler–Lagrange model and the dots are the results of the Euler–Euler model

Downloaded from ascelibrary.org by Universiteit Twente on 05/02/18. Copyright ASCE. For personal use only; all rights reserved.

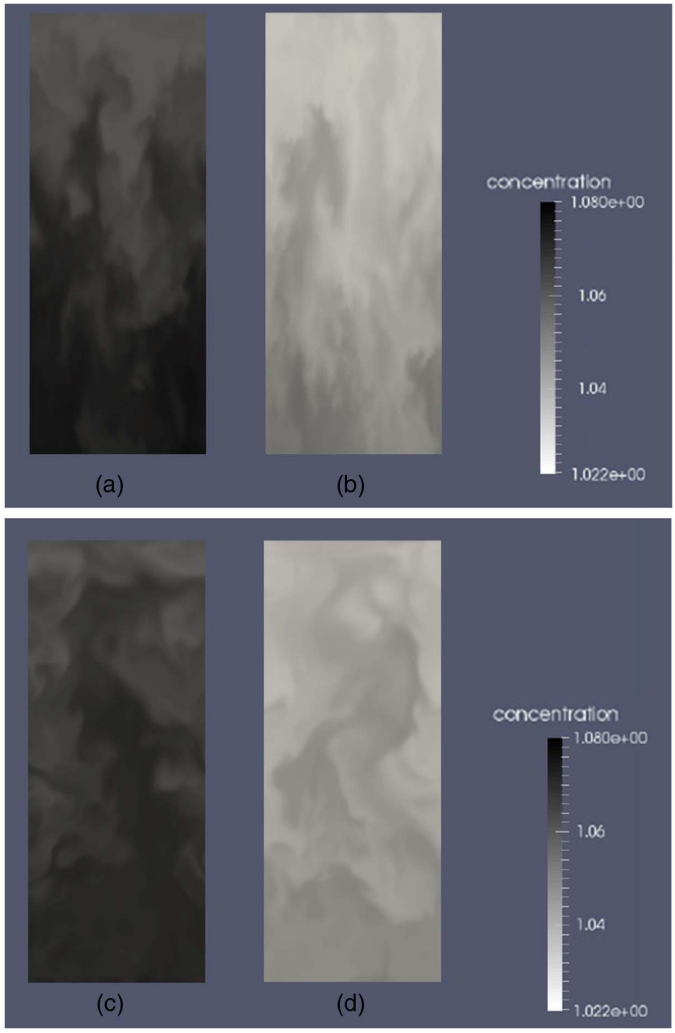

Fig. 3. Dissolved gas concentration (a and c) 300 s and (b and d) 500 s after the start of bubble injection; (a) and (b) are for the Lagrange–Euler model, and (c) and (d) for the Euler–Euler model; the initial bubble diameter is 0.2 mm and the gas flow rate 1.68×10^6 m^3/s, corresponding to 400,000 bubbles per second; the gray scale ranges from 8% supersaturation to 2.2% supersaturation; the initial supersaturation is 30%

the total rate of gas volume injection constant. The quantity shown is the gas concentration averaged over the entire liquid volume as a function of time. The two models gave virtually indistinguishable results, and they both showed a substantial effect of the injected bubbles in rapidly decreasing the liquid gas content. The 0.2-mm bubbles reduced the saturation level basically to saturation in approximately 10 min. When the initial diameter was doubled, and therefore, with the same rate of gas injection, the number of bubbles was reduced by a factor of 8, the rate of decrease of dissolved air slowed but was still sufficient to decrease the initial supersaturation by a factor of nearly 2 in a comparable amount of time.

Snapshots of the concentration fields at $t = 300$ s and $t = 500$ s as given by the two models are shown in Fig. 3. The gray scale ranges from 8.8% supersaturation (dark gray) to 2.2% supersaturation (light gray); the initial concentration was 30% supersaturation. Because this was a time-dependent and fairly irregular flow due to the bubble injection, the concentration fields cannot be compared in detail. However, it is seen here that the two models produced qualitatively fairly consistent results which

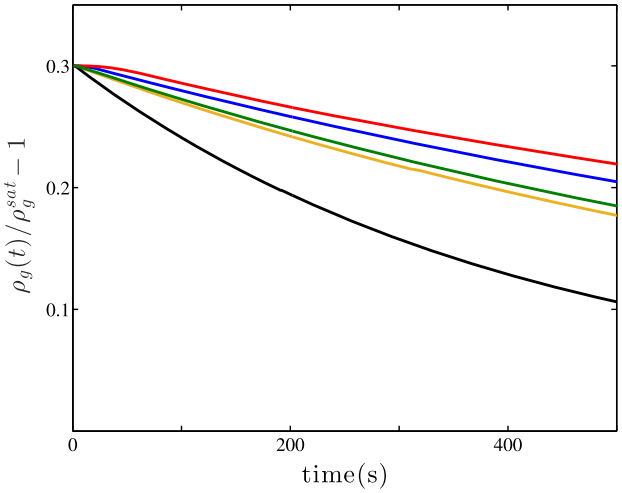

Fig. 4. Decrease of the whole-domain, volume-averaged water supersaturation as a function of time for different initial size of the injected bubbles and the same total number of bubbles injected per unit time, 50,000 per second; the bubble diameters are, in descending order, 0.1, 0.2, 0.4, 0.5, and 1 mm (Euler–Lagrange model)

become indistinguishable upon averaging over the computational domain as shown in Fig. 2.

Fig. 4 is similar to Fig. 2 in that bubbles of different sizes are again compared, but it differs in that the number of bubbles injected per unit time is kept constant irrespective of size. In descending order, the bubble diameters increase from 0.1 to 1 mm. In this case it is the larger bubbles which prove more effective, confirming the considerations made above in connection with Fig. 1: larger bubbles had a faster rise velocity, but the decreased residence time was more than balanced by the larger surface area available for the absorption of gas. A consideration of the time scale again shows the effectiveness of this method for supersaturation reduction.

Figs. 2 and 4 suggest that a compromise between bubble size and injection rate can be reached depending on the specific applications, cost, and available equipment.

Illustrative Results

Further results which illustrate several aspects of the proposed method of supersaturation reduction are given in this section. These results were obtained with the Euler–Euler code in a much larger computational domain, 5 m in height with a square cross section 0.8 m on each side. The initial dissolved gas concentration was 30% above saturation, as before. In order to illustrate the effects of the circulation induced by the rising bubbles, the bubbler was placed at different depths. The bubbler extended only over the central portion of the domain cross section, a square with sides 0.4 m, and bubbles rose by buoyancy, inducing an upward flow of water above the bubbler. This effect drove a circulation inside the domain, with water descending along the lateral boundaries. Driven by this circulation, the supersaturated water below the bubbler moved upward to a higher area, where the local saturation concentration was lower and the bubbles were effective in removing the dissolved gas. Thus, with this arrangement, the bubbler was able to affect the gas concentration both above and below its position.

In the first group of simulations, bubbles were injected at different depths ranging from 2.2 to 4.6 m, while keeping all other parameters constant. The initial bubble diameter was 0.1 mm,

Downloaded from ascelibrary.org by Universiteit Twente on 05/02/18. Copyright ASCE. For personal use only; all rights reserved.

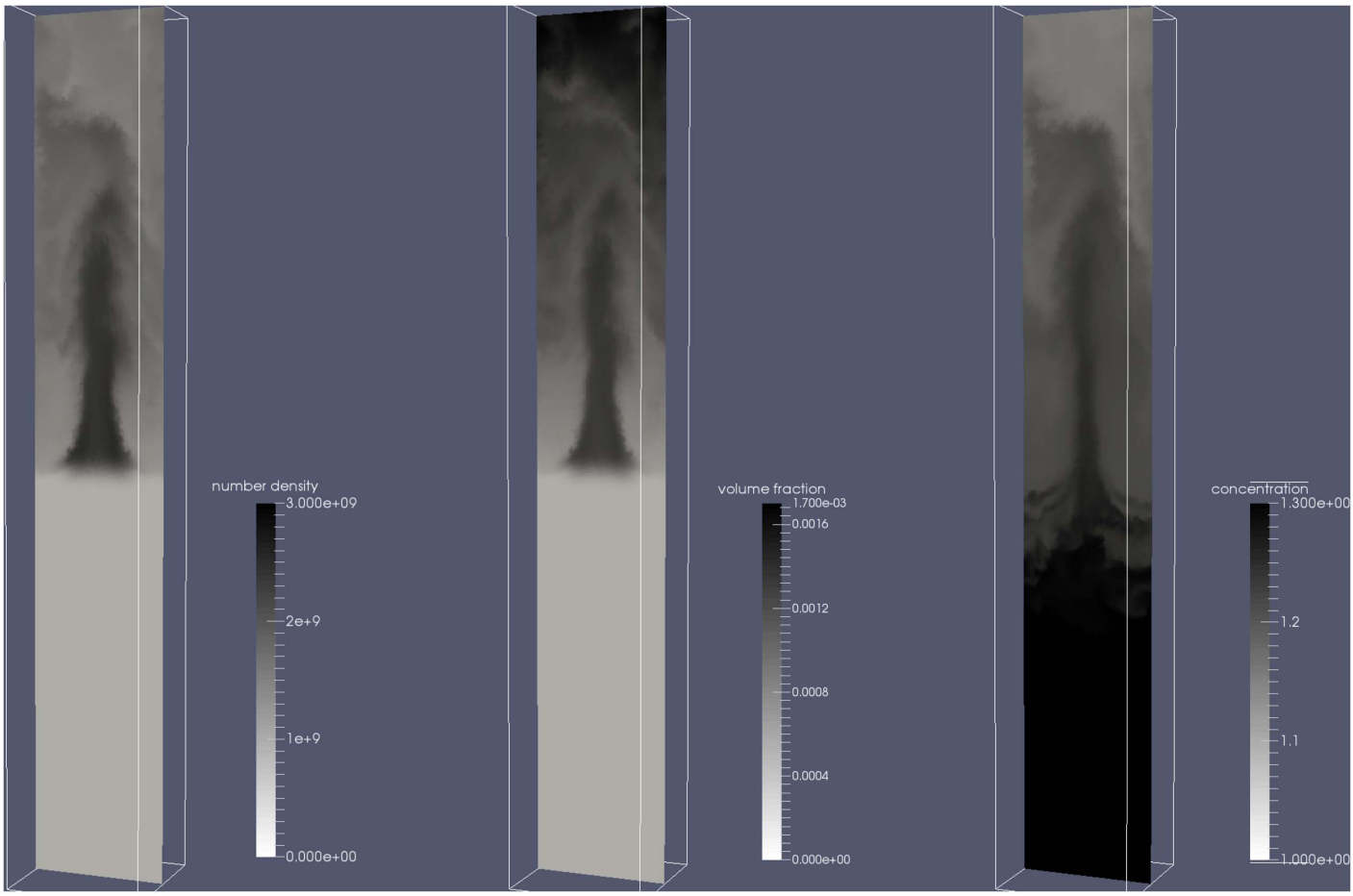

Fig. 5. Three images show snapshots of the bubble number density, volume fraction, and dissolved gas concentration 500 s after the beginning of bubble injection; the gray scale ranges for the bubble number density from 0 to 3×10^9 m^{-3}, for the bubble volume fraction from 0 to 0.17%, and for the dissolved gas concentration from 30% supersaturation to saturation; the depth of the bubbler is 2.6 m, the height of the domain is 5 m, and the initial bubble diameter is 0.1 mm

and the injection volume rate approximately 5.23×10^{-6} m^3/s, corresponding to a bubble generation rate of about 10^7 bubbles per second. The duration of the simulation was 500 s. The second group of simulations studied the effect of the initial bubble diameter, which ranged from 0.1 to 0.5 mm, keeping the depth of the bubbler and the total volume injection rate constant. The bubble volume rate used in this group of simulations was 26.15×10^{-6} m^3/s. The total time simulated was 100 s.

Figs. 5 and 6 show snapshots of the bubble number density, volume fraction, and dissolved gas concentration 500 s after the beginning of bubble injection. In Fig. 5 the bubbler depth was 2.6 m and in Fig. 6 the bubbler depth was 4 m; the initial bubble diameter was 0.1 mm. The bubble number density (leftmost images) was concentrated in the volume directly above the bubbler but, as the volume fraction images show (middle images), there were also bubbles that were carried by the descending recirculation along the sides of the domain. The residence time of these bubbles was greater than those in the central region and, accordingly, they grew larger and gave a large contribution to the volume fraction. The dissolved gas concentration (rightmost images) was generally smaller above the bubbler but it is at first sight somewhat surprising that it appears to be larger in the region of the ascending bubble stream rather than along the sides of the domain. This was caused by the fact that some of the gas-rich liquid under the bubbler was dragged upward by the bubble ascending motion. These concentration images clearly show that gas also was being depleted under the bubbler. The effect was larger at the higher bubbler position because the proximity of the bottom inhibited the motion of the liquid.

Fig. 7, in which the vertical line marks the position of the bubbler, shows the horizontally averaged gas concentration as a function of depth at different instants of time for the simulation of Fig. 5. Once again the gas supersaturation also was affected below the bubbler to a depth of about 1 m.

A global view of the effect of different bubbler depths is given in Fig. 8, which shows the gas concentration averaged over the whole domain as a function of time for different bubbler depths; here the initial bubble diameter is 0.1 mm. The top two lines correspond to the deepest bubbler locations, 4.6 and 3.8 m, which were both below the depth at which the water would be saturated at the prevailing hydrosatitic pressure, namely 3 m. For this reason, the bubbles underwent some dissolution until they had risen enough that they were surrounded by supersaturated water and could start absorbing the dissolved gas. Correspondingly, the overall effect of these bubbles was smaller than for bubbles injected higher up, although, as can be seen, they were also able to reduce the supersaturation.

The purpose of the second group of simulations was to study the effect of bubble size for a given total gas volume flow rate. Fig. 9 shows the horizontally averaged concentration 100 s after the start of bubble injection for initial bubble diameters ranging from 0.1 to

Downloaded from ascelibrary.org by Universiteit Twente on 05/02/18. Copyright ASCE. For personal use only; all rights reserved.

Downloaded from ascelibrary.org by Universiteit Twente on 05/02/18. Copyright ASCE. For personal use only; all rights reserved.

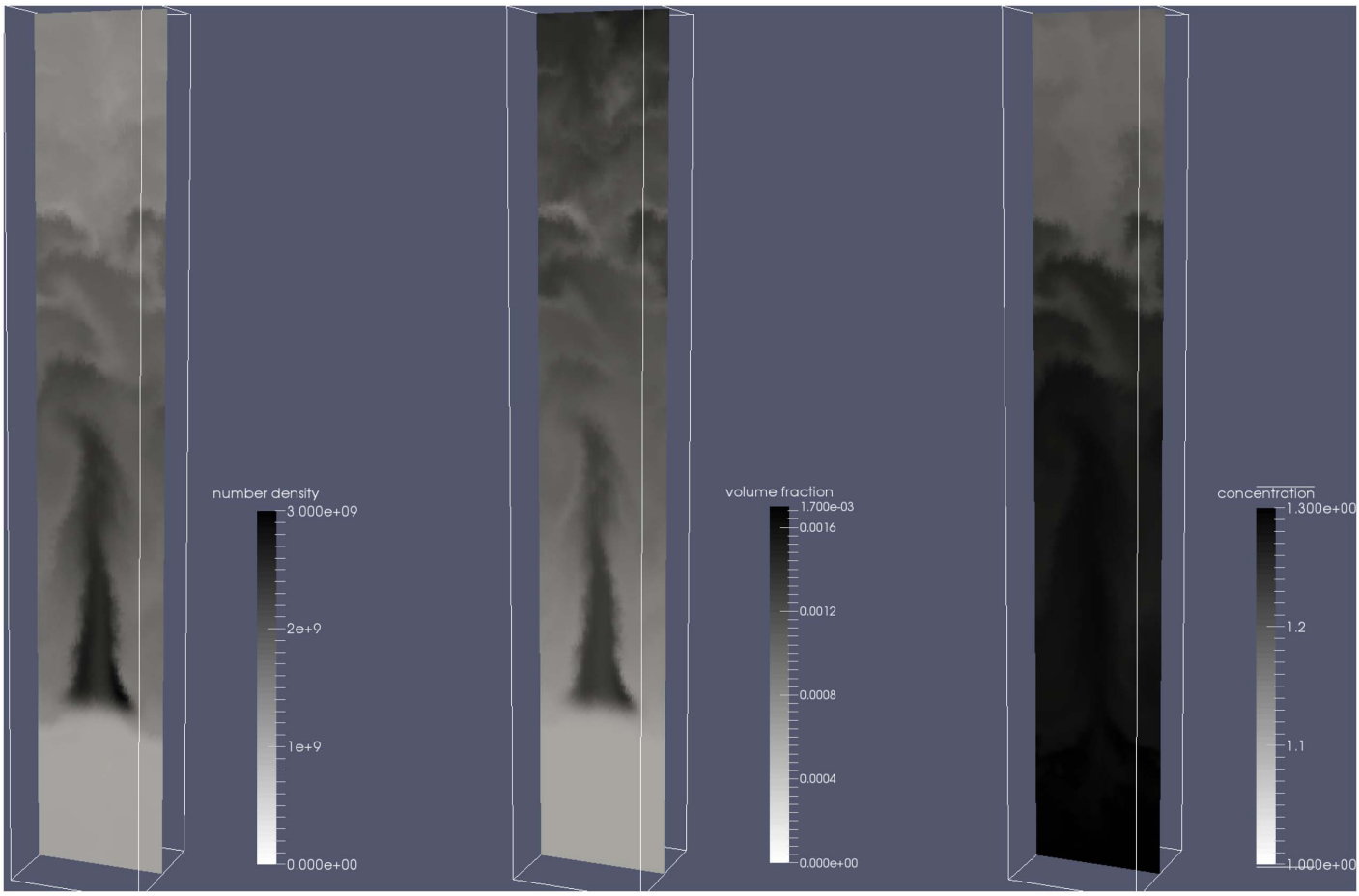

Fig. 6. As in Fig. 5, the three images show snapshots of the bubble number density, volume fraction, and dissolved gas concentration 500 s after the beginning of bubble injection; the gray scale ranges are as in Fig. 5; the depth of the bubbler is 4 m, the height of the domain is 5 m, and the initial bubble diameter is 0.1 mm

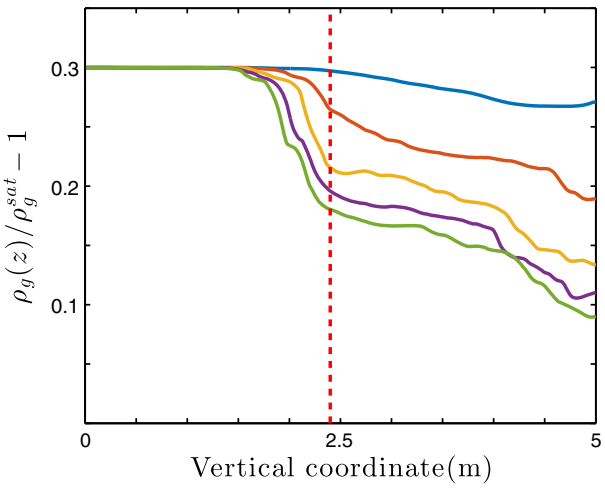

Fig. 7. Average gas concentration over horizontal planes in the water column as a function of vertical distance above the bottom of the domain at, in descending order, $t = 100$, 200, 300, 400, and 500 s; the vertical dashed line is the position of the bubbler, 2.6 m below the surface; the initial bubble diameter is 0.1 mm

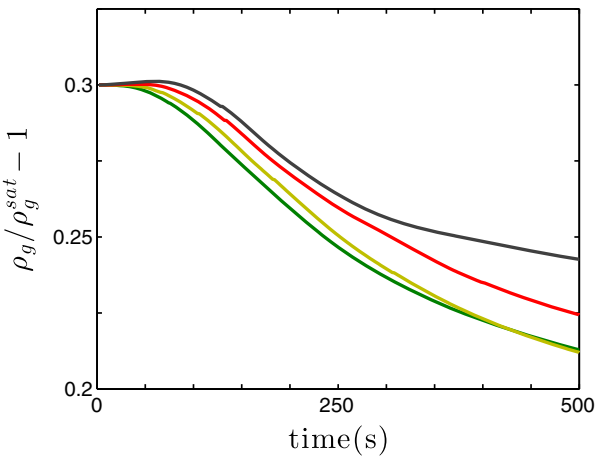

Fig. 8. Whole-domain, volume-averaged dissolved gas concentration as a function of time for simulations with the bubbler positioned, in descending order, 4.6, 3.8, 3, and 2.2 m below the free surface; the initial bubble diameter is 0.1 mm

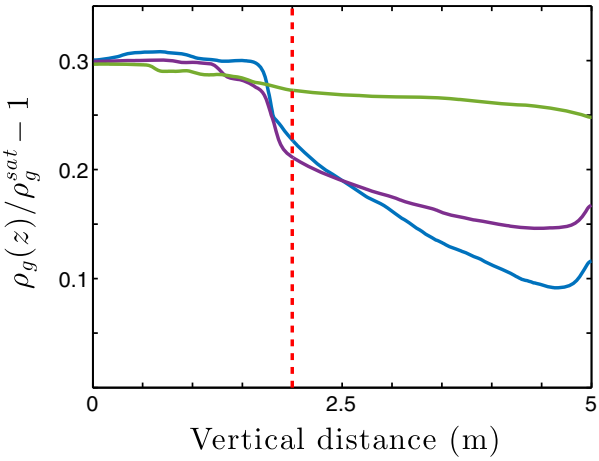

Fig. 9. Average gas concentration over horizontal planes in the water column as a function of vertical distance above the bottom of the domain 100 s after the start of bubble injection; the lines are for initial bubble diameters of, in ascending order, 0.1, 0.2, and 0.5 mm, for the same total gas flow rate; the vertical dashed line is the position of the bubbler, 3 m below the surface

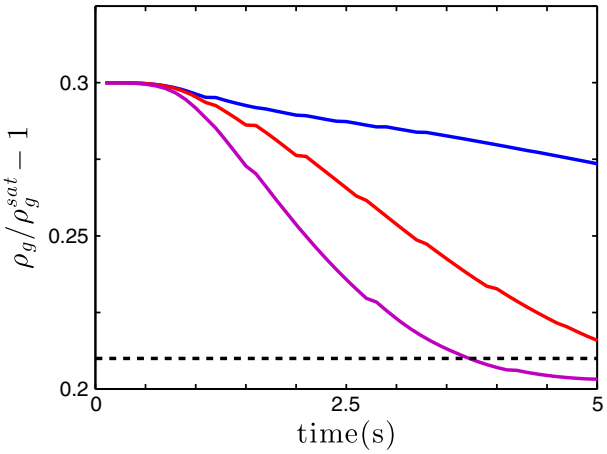

Fig. 11. Whole-domain, volume-averaged dissolved gas concentration as a function of time for simulations with initial bubble diameters of, in ascending order, 0.1, 0.2, and 0.5 mm; the horizontal black dashed line marks the average concentration calculated on the assumption that the liquid above the bubbler is at saturation and the liquid under the bubbler contains the initial uniform concentration

0.5 mm; the bubbler was positioned 3 m below the surface (vertical line). Because the gas flow rate was kept constant, the bubble number increased by about two orders of magnitude as the bubble diameter was reduced from 0.5 to 0.12 mm. As a consequence, the concentration reduction with the largest bubbles was very modest. Other than for the largest bubbles, however, the effect of initial bubble size was not large. This is because, by that time, the gas concentration had been considerably reduced.

The bubble volume fraction as a function of depth at the end of the simulation (100 s) is shown in Fig. 10. As expected, the volume fraction increased with height above the bubbler because the bubbles grew by absorbing the dissolved gas. The effect was smallest for the largest bubbles, but the volume fraction nearly doubled for the other cases with respect to its value on the injection plane.

The time evolution of the volume-averaged dissolved gas concentration for the second group of simulations is shown in Fig. 11. It is interesting to compare this quantity with the average concentration calculated assuming that all the excess gas was removed from the liquid above the bubbler, and the initial concentration remained unchanged in the liquid below (horizontal dashed line). It is remarkable that the smallest bubbles were able to push the average concentration below this level, which implies that not only all the excess gas above the bubbler was removed, but also part of that below the bubbler due to the updraft caused by the ascending bubbles.

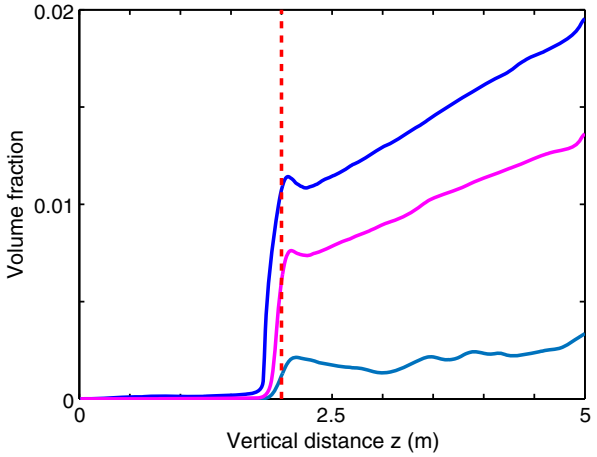

Fig. 10. Average free gas volume fraction over horizontal planes in the water as a function of distance above the bottom of the domain for simulations with initial bubble diameters of, in descending order, 0.1, 0.2 and 0.5 mm; the total gas flow rate is the same in all three cases; the situation depicted occurs 100 s after the start of bubble injection; the vertical dashed line marks the position of the bubbler 2.6 m below the surface

Conclusions

This paper describes the results of a numerical study of the effectiveness of bubble injection as a means to reduce the supersaturation of dissolved air in water. In order to strengthen the results the study used two very different mathematical models and computational codes, finding substantial agreement between the two sets of results. Thus the conclusions reached are robust and little affected by the idealizations unavoidable in a numerical simulation.

The main conclusion is that the proposed method of supersaturation reduction can be very effective and should be studied further. Both bubble size and bubble number play a very significant role. The optimal balance between these two parameters will depend to a large extent on the specific application considered and will also include equipment and energy costs, methods of deployment, and other factors. Therefore no attempt has been made here to determine it. A general conclusion, however, is that, for a fixed total gas flow rate, bubbles with a diameter of about 0.1 mm are most effective. Effectiveness declines as the bubble diameter is increased, fairly slowly initially but gradually more rapidly as millimeter-size is approached.

It should be noted that the generation of submillimeter bubbles does not necessarily require the use of small pores, which are notoriously prone to occlusion. The problem is especially severe in difficult-to-control settings, such as rivers and other water bodies.

Downloaded from ascelibrary.org by Universiteit Twente on 05/02/18. Copyright ASCE. For personal use only; all rights reserved.

Very small bubbles can be generated in a Venturi nozzle by using shearing forces between the water flowing through the nozzle and the air emerging from an opening near the throat of the nozzle (e.g., Kaneko et al. 2012; Yin et al. 2015). The flow passages required by this method are orders of magnitude larger than the bubbles being produced and occlusion problems are therefore greatly mitigated.

Acknowledgments

The authors are grateful to Prof. Joe Katz for useful discussions. This work has been supported by Grant No. R14AP00151 from the U.S. Bureau of Reclamation.

References

Beiningen, K. T., and Ebel, W. J. (1970). "Effect of John Day Dam on dissolved nitrogen concentrations and salmon in the Columbia River, 1968." *Trans. Am. Fish. Soc.*, 99(4), 664–671.

Capecelatro, J., and Desjardins, O. (2013). "An Euler-Lagrange strategy for simulating particle-laden flows." *J. Comput. Phys.*, 238(1), 1–31.

Ebel, W. J. (1969). "Supersaturation of nitrogen in the Columbia River and its effect on salmon and steelhead trout." *Fishery Bull.*, 68(1), 1–11.

Feng, J., Li, R., Liang, R., and Shen, X. (2014). "Eco-environmentally friendly operational regulation: An effective strategy to diminish the TDG supersaturation of reservoirs." *Hydrol. Earth Syst. Sci.*, 18(3), 1213–1223.

Ferziger, J., and Periç, M. (2002). *Computational methods for fluid dynamics*, 3rd Ed., Springer, Berlin.

Fletcher, C. A. J. (1988). *Computational techniques for fluid dynamics*, Springer, Berlin.

Gunnarsli, K. S., Toften, H., and Mortensen, A. (2008). "Effects of nitrogen gas supersaturation on growth and survival in juvenile Atlantic cod (*Gadus morhua* L.)." *Aquaculture*, 283(1–4), 175–179.

Hansen, K. M., Mesa, M. G., and Maule, A. G. (1999). "Rate of disappearance of gas bubble trauma signs in juvenile salmonoids." *J. Aquatic Anim. Health*, 11(4), 383–390.

Hochbruck, M., and Ostermann, A. (2010). "Exponential integrators." *Acta Numer*, 19, 209–286.

Huang, X., Li, K.-F., Du, J., and Li, R. (2010). "Effects of gas supersaturation on lethality and avoidance responses in juvenile rock carp (*Procypris rabaudi* Tchang)." *J Zhejiang Univ. Sci. B*, 11(10), 806–811.

Ireland, P. J., Vaithianathan, T., Sukheswalla, P. S., Ray, B., and Collins, L. R. (2013). "Highly parallel particle-laden flow solver for turbulence research." *Comput. Fluids*, 76(1), 170–177.

Johnson, E., Clabough, T., Peery, C., Bennett, D., Bjornn, T., and Stuehrenberg, L. (2004). "Migration depths of adult spring–summer chinook salmon in the lower Columbia and Snake Rivers in relation to dissolved gas supersaturation." *Technical Rep. 2004-8*, Idaho Cooperative Fish and Wildlife Research Unit, Univ. of Idaho, Moscow, ID.

Kaneko, A., Gong, X., Takagi, S., and Matsumoto, Y. (2012). "Development of microbubble generator and its utilization to enhance the mass transfer in the bubble plumes and columns." *Proc., ASME Fluids Engineering Division Summer Meeting*, Puerto Rico, 191–196.

Knittel, M. D., Chapman, G. A., and Garton, R. R. (1980). "Effects of hydrostatic pressure on steelhead survival in air-super-saturated water." *Trans. Am. Fish. Soc*, 109(6), 755–759.

Liu, X. Q., Li, K. F., Jiang, W., and Wu, S. (2015). "Biochemical responses and survival of rock carp (Procypris rabaudi) to total dissolved gas supersaturated water." *Ichthyol. Res.*, 62(2), 171–176.

McGrath, K., Dawley, E. M., and Geist, D. R. (2006). "Total dissolved gas effects on fishes of the lower Columbia river." *Technical Rep. PNNL-15525*, Pacific Northwest National Laboratory, Richland, WA.

Meekin, T. A., and Turner, B. K. (1974). "Tolerance of salmonid eggs, juveniles, and squawfish to supersaturated nitrogen." *Technical Rep. 12*, Washington Dept. of Fisheries, Olympia, WA, 75–126.

Oresta, P., and Prosperetti, A. (2013). "Effects of particle settling on Rayleigh-Bénard convection." *Phys. Rev. E*, 87(6), 063014.

Pickett, P. J., and Harding, R. (2002). "Total maximum daily load for lower Columbia River total dissolved gas." *Technical Rep. Publication No. 02-03-004*, Washington State Dept. of Ecology, Lacey, WA.

Skov, P. V., Pedersen, L.-F., and Pedersen, P. B. (2013). "Nutrient digestibility and growth in rainbow trout (*Oncorhynchus mykiss*) are impaired by short term exposure to moderate supersaturation in total gas pressure." *Aquaculture*, 416(2), 179–184.

Wang, Y., Li, K. F., Li, J., and Deng, Y. (2015). "Tolerance and avoidance characteristics of Prenant's Schizothoracin Schizothorax prenanti to total dissolved gas supersaturated water." *North. Amer. J. Fisheries Manage.*, 35(4), 827–834.

Weitkamp, D. E., and Katz, M. (1980). "A review of dissolved gas supersaturation literature." *Trans. Am. Fish. Soc.*, 109(6), 659–702.

Yin, J. L., Li, J. J., Li, H., Liu, W., and Wang, D. Z. (2015). "Experimental study on the bubble generation characteristics for a Venturi type bubble generator." *Int. J. Heat Mass Transfer*, 91(2), 218–224.

Downloaded from ascelibrary.org by Universiteit Twente on 05/02/18. Copyright ASCE. For personal use only; all rights reserved.